Atmospheric Research 275 (2022) 106217

Contents lists available at ScienceDirect

Atmospheric Research

journal homepage: www.elsevier.com/locate/atmosres

Comparison of CIMEL sun-photometer and ground-based GNSS integrated water vapor over south-western European sites

Javier Vaquero-Martínez [a,b,*], André F. Bagorrilha [a,b], Manuel Antón [a,b], Juan C. Antuña-Marrero [c], Victoria E. Cachorro [c]

[a] Department of Physics, University of Extremadura, Badajoz, Spain
[b] Instituto Universitario de Investigación del Agua, el Cambio Climático y Sostenibilidad, University of Extremadura, Badajoz, Spain
[c] Group of Atmospheric Optics (GOA-UVa), Universidad de Valladolid, 47011 Valladolid, Spain

ARTICLE INFO

Keywords:
Water vapor
Sun-photometer
GNSS
Comparison

ABSTRACT

This work analyzes the integrated water vapor (IWV) measured at six Aerosol Robotic Network (AERONET) stations with nearby global navigation satellite system (GNSS) in the Iberian Peninsula for the period 2007–2018. It is shown that both instruments have a high correlation ($R^2 > 0.91$), with small mbe below 1.5 mm and standard deviation (SD) below 2 mm. However, some dependences have been observed when MBE and SD are represented in bins of three variables: IWV, solar zenith angle (SZA), and aerosol optical depth (AOD). The greater or lesser amount of water vapor in the atmosphere seemed to be the more influential variable, increasing dry bias and SD with increasing IWV. Moreover, high SZA values were related to SD increases. A clear seasonal cycle for Cimel–GNSS differences was observed which was mainly related to IWV seasonal cycle. Additionally, AOD did not show a remarkable influence on Cimel–GNSS differences. Finally, the monthly differences are also analyzed with metadata information about Cimel device ID numbers, showing that, for long-term studies, this information can be very valuable.

1. Introduction

Among the different trace gases in the atmosphere, water vapor is considered of paramount importance due to its relevant roles in many proceses. It is key to the dynamics of the troposphere and also regarded as the most important natural greenhouse gas (Myhre et al., 2013). Particularly, is the major absorbent of long-wave radiation and its role in the climate system is considered a positive feedback (Colman, 2003, 2015).

Water vapor can be studied through many variables (relative humidity, specific humidity, partial pressure, …), and the commonly used integrated water vapor (IWV), which is defined as the integral of the concentration of water vapor along the vertical path, being its units those of superficial density (kg m^{-2}). This can also be defined as the height that water would reach if all of it condensated in a vessel of the same cross-section as the atmospheric column. Taking into account the density of liquid water, the unit of height (mm) is equivalent to the one of superficial density. For this reason, IWV is also known as precipitable water vapor.

The measurements of IWV typically show a high variability in the temporal domain, as well as in the spatial one. It is, therefore, necessary to measure this variable with high temporal and spatial resolution in order to monitor it adequately. However, no instrument by itself can catch both the temporal and spatial variability. Hence, it is fundamental to use different kinds of instruments to study water vapor, have coincident measurements to understand their uncertainties better, and be aware of their limitations and strengths to design research in the most proper manner.

Particularly, water vapor retrieval from ground-based global navigation satellite system (GNSS) data is a recent, high quality technique which is commonly used in comparisons and validations of instruments as a reference (Bennouna et al., 2013; Bock and Nuret, 2009; Carbajal Henken et al., 2020; Cucurull et al., 2000; Gong et al., 2019; Köpken, 2001; Matsuyama et al., 2020; Ningombam et al., 2016; Raja et al., 2008; Román et al., 2015; Vaquero-Martínez et al., 2017a, 2017b, 2018, 2020; Wang et al., 2016, 2019; Yang et al., 1999). Among its advantages, it is worthy of note that there exists dense networks of GNSS receivers around the world (not in all countries and certainly not over oceans).

* Corresponding author at: Department of Physics, University of Extremadura, Badajoz, Spain.
E-mail address: javier_vm@unex.es (J. Vaquero-Martínez).

https://doi.org/10.1016/j.atmosres.2022.106217
Received 4 January 2022; Received in revised form 31 March 2022; Accepted 22 April 2022
Available online 28 April 2022

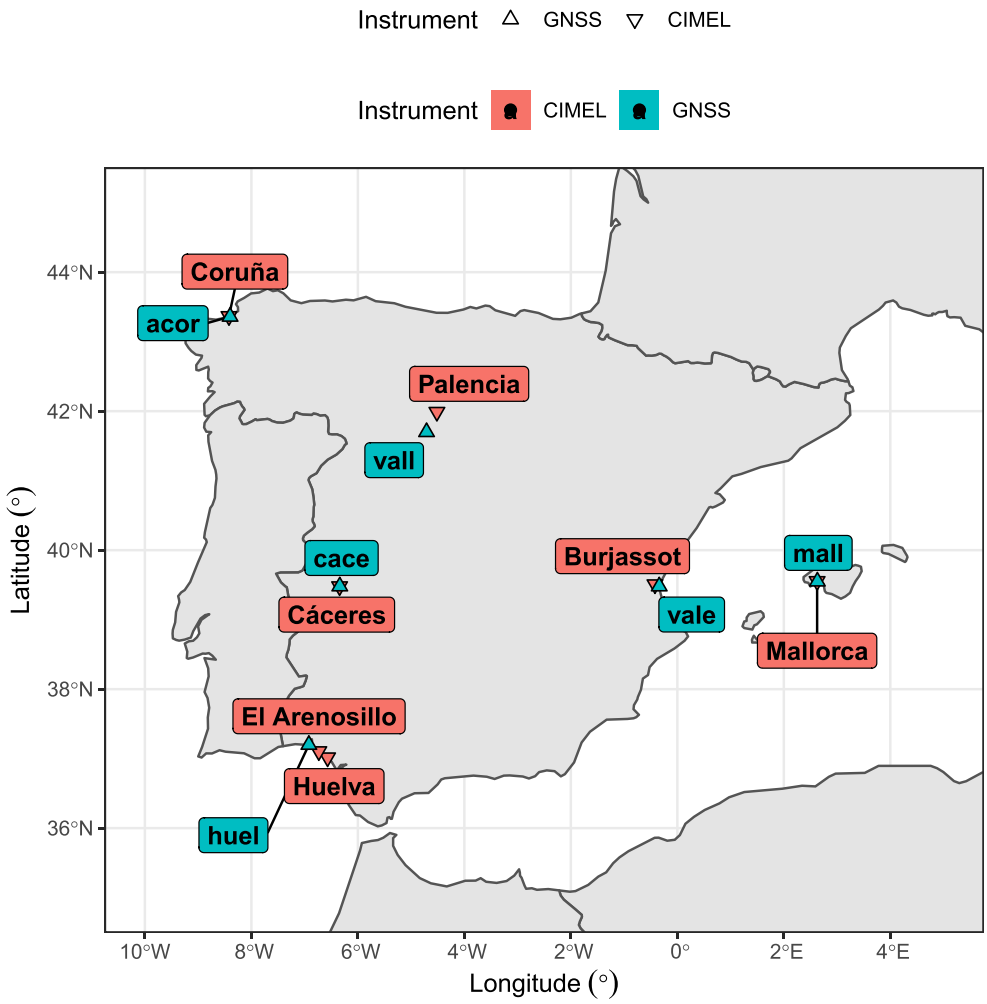

Fig. 1. Map showing the location of the stations selected for the study.

Moreover, the networks are easily maintained and the data can be obtained under all-weather conditions (Vaquero-Martínez and Antón, 2021).

The Aerosol Robotic Network (AERONET) (Holben et al., 1998) is a worldwide network of ground-based stations devoted to the study of aerosols. Their main instrument is the Cimel sun-photometer, which allows the retrieval of many aerosol properties but it also provides information about water vapor in the form of IWV (Fragkos et al., 2019; Pérez-Ramírez et al., 2014; Schneider et al., 2010; Antuña-Marrero et al., 2022). This is achieved by pointing the photometer to the sun and, under direct sunlight, record the amount of radiation in several wavelength bands. Therefore, this technique requires the presence of sunlight at the moment of measurement, discarding nighttime and cloudy-sky scenarios. AERONET also archives these measurements with high quality standards and homogeneity in the measurements. Recently, a new Version 3 (V3) of AERONET data has been released with an improved algorithm, which is worth testing.

The Iberian Peninsula is an interesting region of study, as it exhibits different meteorological conditions in different regions and has a extensive network both in GNSS and Cimel sun-photometers within AERONET. Therefore, this work focuses on the validation of the newly released V3 of the AERONET photometer network in six Spanish stations that count with GNSS stations nearby. Section 2 describes the data needed for this work, while Section 3 summarizes the methodology applied. The results are presented and discussed in Section 4, and the conclusions are drawn in Section 5.

Table 1
Sites of Cimel and GNSS and their locations. It must be noted that Huelva and El Arenosillo Cimel stations are both matched to *huel* GNSS station. The period for El Arenosillo spans from 200709-10 to 2010-03-04, while Huelva period goes from 201003-18 to 2015-10-09.

Cimel				GNSS			
Station	Lat (°)	Long (°)	Elev (m)	Station	Lat (°)	Long (°)	Elev (m)
Palencia	41.99	−4.52	750	vall	41.70	−4.71	766
Burjassot	39.51	−0.42	30	vale	39.48	−0.34	28
Mallorca	39.55	2.63	10	mall	39.55	2.63	62
Huelva	37.02	−6.57	25	huel	37.20	−6.92	29
El Arenosillo	37.10	−6.73	59	huel	37.20	−6.92	29
Cáceres	39.48	−6.34	397	cace	39.48	−6.34	384
Coruña	43.37	−8.42	67	acor	43.36	−8.40	12

2. Data

Six stations in Spain from AERONET (Holben et al., 1998) were selected, as those were the ones with close GNSS ground-based stations. The six stations are depicted in Fig. 1, while their locations and corresponding nearby GNSS stations can be found in Table 1.

2.1. Cimel sun photometer data

The AERONET water vapor product is the V3 and only data with level 2.0 (highest quality) are considered in this work. The standard instrument of AERONET is the Cimel CE-318 photometer. It carries out solar radiation measurements at different wavelengths in the range 340 nm to 1020 nm. The instrument is described in depth in (Holben et al., 1998). The data were downloaded from the aeronet website (https://aeronet.gsfc.nasa.gov/cgi-bin/webtool_aod_v3).

The retrieval approach deals with the attenuation of radiation according to the Beer-Bouger-Lambert law. The retrieval method is described in the following lines. A more detailed description can be found in García et al. (2021). The response of the instrument can be modeled by the following expression:

$$\mathrm{DNI}(\lambda) = \mathrm{DNI}_0(\lambda) \cdot exp(-\tau(\lambda) \cdot m) T_w(\lambda) \tag{1}$$

where $\mathrm{DNI}(\lambda)$ is the direct normal irradiance at wavelength λ, $\mathrm{DNI}_0(\lambda)$ is the same but at the top of atmosphere, $\tau(\lambda)$ is the optical depth, m is the optical air mass, and $T_w(\lambda)$ is the water vapor transmittance. The main contributions of $\tau(\lambda) \cdot m$ are the Rayleigh scattering (see Hansen and Travis, 1974; Kasten and Young, 1989, for descriptions on the modeling of this contribution) and the aerosol extinction, calculated according to Ångström (1961); Kasten (1965).

The water vapor transmission is related to the IWV. This relation was studied by Bruegge et al. (1992); Halthore et al. (1992).

$$T_w(\lambda) = exp\left(-a(m_w \cdot \mathrm{IWV})^b\right) \tag{2}$$

The water vapor optical mass m_w is approximately equal to that of the aerosols. The constants a and b are dependent on the wavelength, shape and width of the filter functions, pressure and temperature, and vertical distribution of water vapor.

This way, the IWV can be obtained as

$$\mathrm{IWV} = \frac{1}{m_w}\left[\frac{1}{a}\left(ln\frac{\mathrm{DNI}_0}{\mathrm{DNI}} - \tau(\lambda)m\right)\right]^{\frac{1}{b}} \tag{3}$$

With this approach, the one sigma uncertainty is expected to be below 10% in comparison to GNSS IWV (Giles et al., 2019).

2.2. GNSS data

gnss data are obtained, hourly at XX:30 UTC, for 6 stations nearby the selected sun-photometer stations, as shown in Table 1 and Figure1. GNSS water vapor retrieval is based on Bevis et al. (1992, 1994). Here, we describe the fundamental steps in this approach. GNSS processing for acquisition of a receiver's position needs to account for the delay of the signal caused by its passing through the troposphere. This quantity is typically multiplied by the velocity of light and presented in length units. Here, we describe the fundamental steps in this approach. GNSS processing for acquisition of a receiver's position needs to account for the delay of the signal caused by its passing through the troposphere. This quantity is typically multiplied by the velocity of light and presented in length units. When the tropospheric delay is measured in the satellite-receiver direction, it is called slant total delay (STD). However, being this quantity dependent on the satellite-receiver geometry, this is usually converted to the zenith direction using mapping functions. The converted quantity is called zenith total delay (ZTD). ZTD is the sum of two contributions, one caused by water vapor only, known as zenith wet delay (ZWD) and another one caused by all the tropospheric gases, known as zenith hydrostatic delay (ZHD). The ZHD is calculated using the model proposed by Elgered et al. (1991) and Saastamoinen (1972), whose inputs are the pressure at the station level (P_s, in hPa), the height of the station above the ellipsoid (H, in km) and the latitude (λ) of the station

$$\mathrm{ZHD} = 0.0022768 \frac{P_s}{1 - 0.00266cos2\lambda - 0.00028H} \tag{4}$$

The pressure at the station level is obtained from automatic meteorological stations nearby each GNSS site, interpolated to the time of the measurement taking into account the effect of the barometric tide. The pressure is also reduced to the height of the GNSS site. Moreover, obtaining the ZHD allows the computation of ZWD by subtraction ZWD = ZTD − ZHD. Then, the IWV can be obtained as:

$$\mathrm{IWV} = \kappa \mathrm{ZWD} \tag{5}$$

$$\kappa = \frac{1 \times 10^6}{\rho R_v \left(\frac{k_3}{T_m} + k_2'\right)} \tag{6}$$

κ is a conversion factor which can be calculated from mean temperature (T_m; Davis et al., 1985), ρ is the density of water, R_v is the gas constant of water vapor, k_3 is a refraction constant and $k_2' = k_2 - mk_1$, being m the ratio between water vapor and dry air molar mass and k_2 and k_1 are refraction constants. The Davis mean temperature is defined as

$$T_m = \frac{\int \frac{P_v}{T} \mathrm{d}z}{\int \frac{P_v}{T^2} \mathrm{d}z} \tag{7}$$

P_v is water vapor partial pressure, T is temperature, and z is height. T_m is usually obtained as a linear regression estimate ($T_m = 61.9 + 0.75\ T_s$ in our case, see Ortiz de Galisteo et al., 2011) from surface temperature from close meteorological stations. However, the diurnal cycle of surface temperature is more marked than that of T_m and therefore the T_s is replaced by a smoothed temperature T_{ss} which is calculated as a weighted average between surface temperature and daily mean temperature ($T_{ss} = 0.25 \cdot T_s + 0.75 \cdot T_{\mathrm{dailymean}}$). This follows the methodology proposed by Morland et al. (2009) which avoids the induction of artificial daily cycle. Hourly surface temperature is obtained from national meteorological agency (AEMet) in Spain, converted to the height of the stations (assuming a lapse rate of −6.5°C/km). Surface atmospheric pressure is also obtained from AEMet (also reduced to GNSS station heights) and ZTD data are obtained from EUREF Permanent Network.

The GNSS data processing is carried out by local analysis centre IGE (Spanish Geographic Institute) with Bernese GPS software, using double differences with ionosphere-free linear combination and Niell mapping function between 1400 and 1755 weeks, and Global Mapping Function (GMF) from week 1756 to week 1980, and elevation cutoff angle of 10°, and absolute antenna calibrations. GPS was the only system up to week 1756, when Russian GNSS (GLONASS) was added to the processing. From week 2020, Galileo was added as well. More information about this retrieval approach can be found in Ortiz de Galisteo et al. (2011), which had been previously tested with excellent results in Ortiz de Galisteo et al. (2010), improving previous data obtained with relative calibrations of the GNSS antenna.

The assessment of the quality of GNSS water vapor retrievals has been widely studied. However, extensive literature research (Buehler et al., 2012; Bock et al., 2021) showed that the results of comparisons in terms of offset and slope are very dependent on the study (instruments, regions of study, periods, data processing strategies, and so on) and, therefore, no pattern can be found. In any case, systematic differences are typically observed in the 1 mm to 2 mm range. Moreover, it has been observed that GNSS have low sensitivity to small amounts of water

Table 2
General statistics for the comparison. MBE, SD and y0 are in mm, while rMBE and rSD are in percentage. Slope, R2 and n are unitless. The IWV column shows the mean GNSS IWV in mm.

Site	MBE	SD	rMBE	rSD	IWV	n	y0	slope	R2
acor	+0.52	1.29	+3.98	7.81	17.73	9650	+1.08	0.97	0.96
cace	−0.55	1.46	−1.48	10.60	14.69	9965	+1.49	0.86	0.95
huel	−0.18	1.87	+0.66	11.74	17.51	16,182	+1.62	0.90	0.92
mall	+0.83	1.50	+4.59	7.60	21.23	15,367	+0.73	1.00	0.97
vall	−1.48	1.72	−8.78	11.79	14.24	15,070	+0.98	0.83	0.92
vale	−0.65	1.48	−2.71	7.75	20.05	22,601	+0.35	0.95	0.97

vapor, which causes a systematic overestimation of this instruments under dry situations (Wang et al., 2007; Schneider et al., 2010). Under low humidity conditions, the ZTD is mostly due to the hydrostatic contribution. Hence, the uncertainty in the calculation of ZTD leads to a large relative error in ZWD.

Additionally, aerosol optical depth (AOD) data at 551 nm are retrieved from the same AERONET dataset.

3. Methodology

For each site, data from sun-photometer is averaged within ±30 min window around the GNSS measurement.

The distribution of the differences photometer-GNSS are studied. For each instant i and site s, the differences (δ) and relative differences ($\delta(\%)$):

$$\delta_{i,s} = \mathrm{IWV}_{i,s}^{\mathrm{photometer}} - \mathrm{IWV}_{i,s}^{\mathrm{GNSS}} \tag{8}$$

$$\delta_{i,s}(\%) = 100 \cdot \frac{\delta_{i,s}}{\mathrm{IWV}_{i,s}^{\mathrm{GNSS}}} \tag{9}$$

Then, the distribution of these differences is analyzed. Moreover, linear regression models are established in each site, to study the proportionality of the two data-sets. In addition to this, the dependences of these differences on three variables (IWV, solar zenith angle (SZA) and

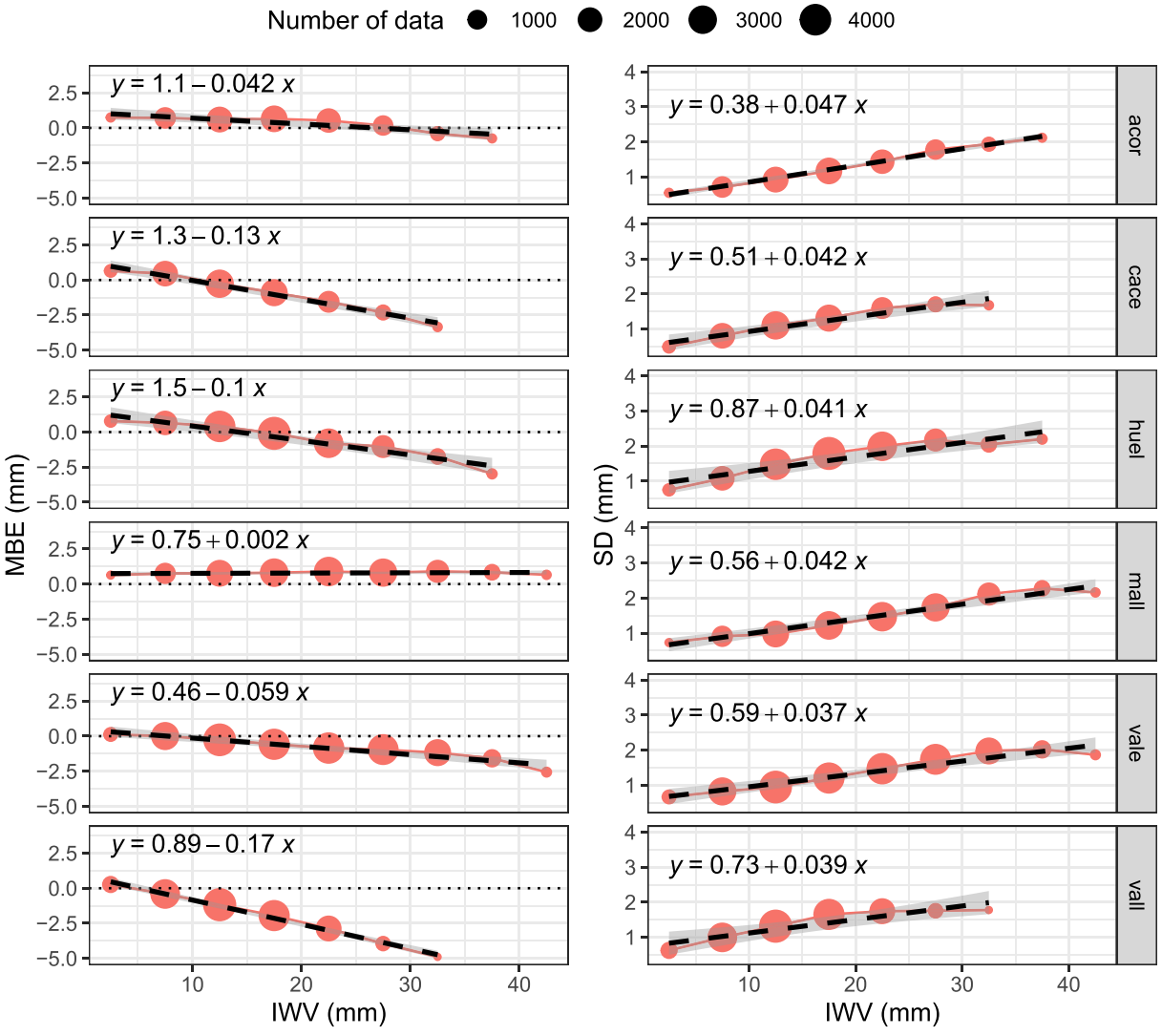

Fig. 2. MBE (left panels) and SD (right panels) along IWV values. Dashed line represents the linear fit.

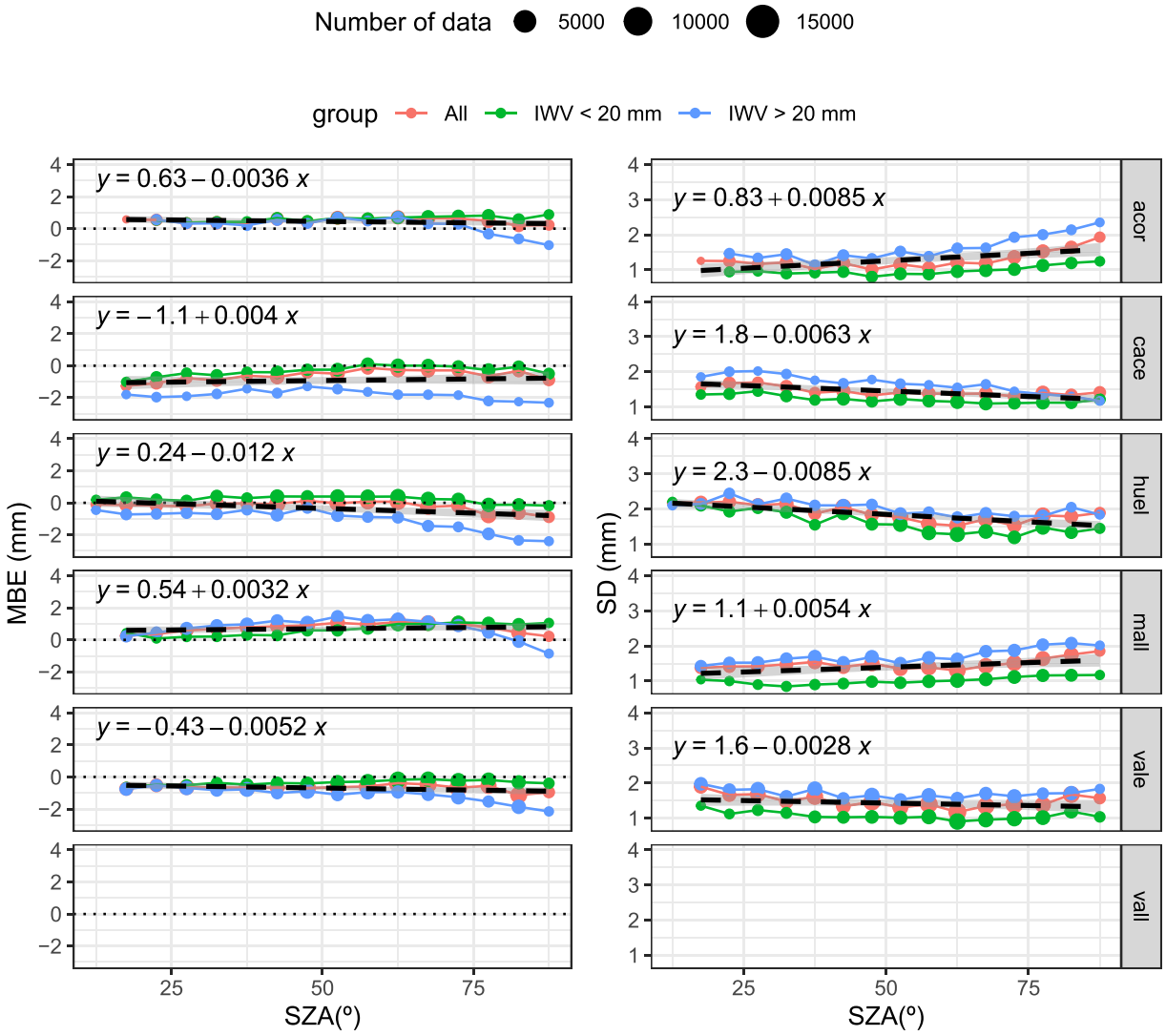

Fig. 3. MBE (left panels) and SD (right panels) along SZA values. Dashed line represents the linear fit.

AOD) are studied. To achieve this, the data is divided into bins of the study variable, and some statistical indexes are applied to the differences in each bin. This is represented along the analyze variable to study the evolution of the indices (Y-axis) along the range of the study variable (X-axis). The selected indices are: mean bias error (MBE), standard deviation (SD), defined as

$$\mathrm{MBE} = \frac{1}{N}\sum_i \delta_i \tag{10}$$

$$\mathrm{SD} = \sqrt{\frac{1}{N-1}\sum_i (\delta_i - MBE)^2} \tag{11}$$

In these equations, N is the number of data pairs and i is an index that represents each of these pairs. Thus, MBE represents the bias of the data (positive if Cimel overestimates measurements and negative if it underestimates them), and SD represents the precision of the data (if the differences are close to the mean value or more disperse around it). For clarity, when these indices are calculated over the relative differences, we will call them relative mean bias error (rMBE) and relative standard deviation (rSD).

4. Results and discussion

4.1. General statistics

Some statistics are shown in Table 2. MBE and SD show the mean and standard deviation of the differences, while the prefix *r* indicates that the indices are applied over the relative differences. It is observed that MBE are negative in most sites (four) and positive in two of them. In all cases the bias is less than 1 mm, except in the case of *vall* (−1.5 mm). Regarding the relative differences, rMBE is more variable, ranging from −8.78% (*vall*) to +4.59% (*mall*). This dry bias of Cimel is consistent with the one found in Barcelona by Campmany et al. (2010, 180 data-points), but in that case it was stronger (−2.62 mm). In the case of Fragkos et al. (2019) at a station close to Bucharest (Romania), the comparison of Cimel and radiosonde showed similar results to the present work (−0.39 mm or −1.95%, with 565 data points for V3 data). Pérez-Ramírez et al. (2014) found also a dry bias of Cimel (Version 2 (V2) AERONET data) both against GPS (−0.8 mm) and radiosonde (−0.4 mm) in different stations around the world. It is clear that Cimel tend to exhibit a dry bias, but the value of such bias is more discussed and probably differences both in methodology and the conditions of the different set-ups (meteorological characteristics of the site, different calibration/photometers, and so on) can influence the resulting value of MBE in the comparisons

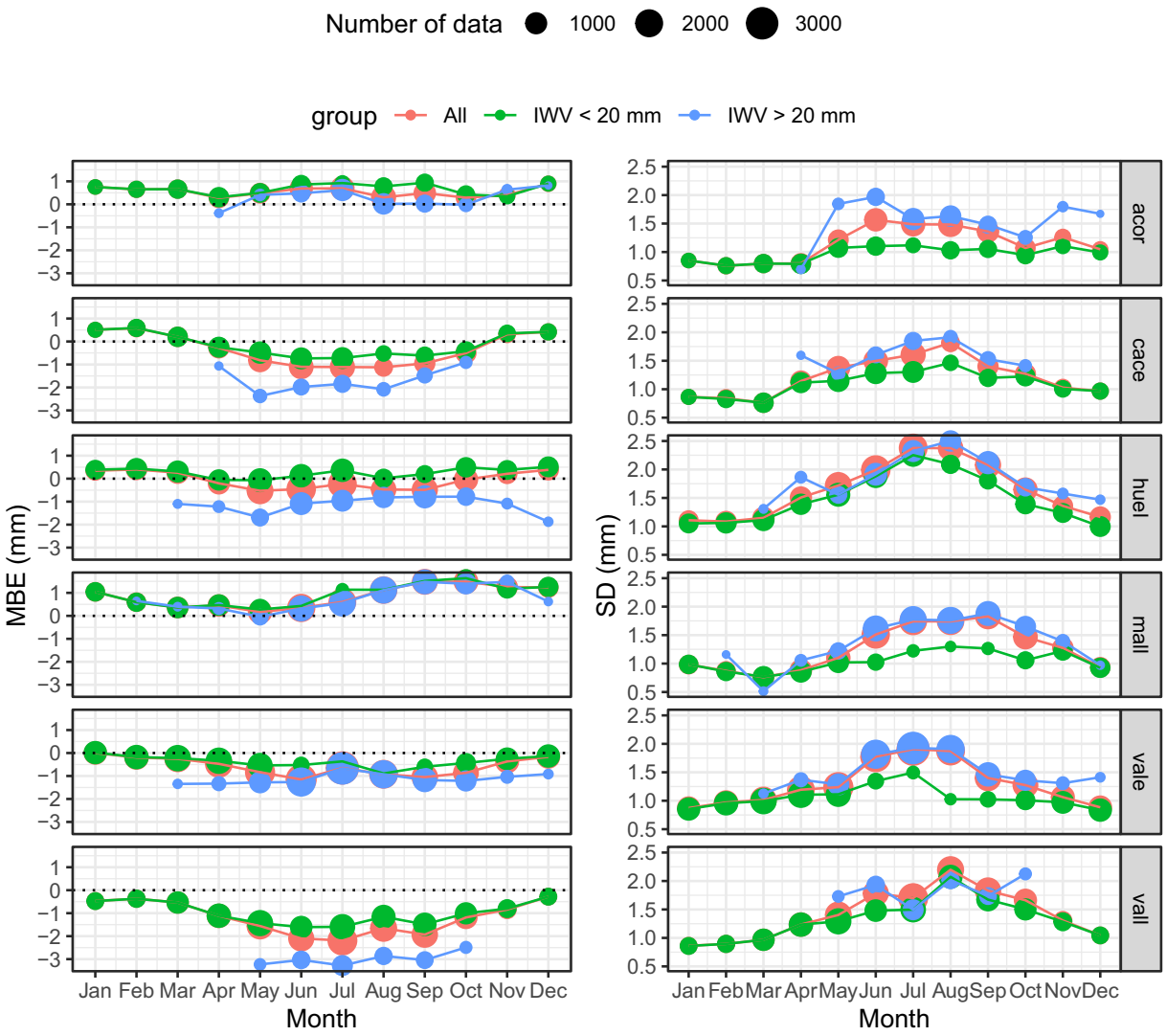

Fig. 4. MBE (left panels) and SD (right panels) along the year.

of Cimel sun-photometers with other instrumentation. In any case, the MBE is in line with the expected uncertainties of Cimel and GNSS instruments.

SD values are below 2 mm in all cases, while rSD values are more similar, with values between 7.8% and 11.8%. Other works agree with these values, such as Campmany et al. (2010, 1.76 mm or 12.29 %), Fragkos et al. (2019, 2.10 mm or 10.97 %), Pérez-Ramírez et al. (2014, 0.7 to 3.0 mm).

Regarding linear regression, the intercepts are positive for all sites, going from 0.35 mm (*vale*) to 1.62 mm (*huel*). The positive intercepts are observed in other works as well, and in part related to GNSS underestimation for low IWV values (Wang et al., 2007; Schneider et al., 2010). However, the slopes are lower or equal to the ideal (the unit) in all cases. The lower is 0.83 in the case of *vall*. Similar behavior was found by Pérez-Ramírez et al. (2014). However, in that work the inverse regression is performed (X is Cimel and Y is GNSS), and therefore, it is difficult to compare the results. All determination coefficients R^2 are 0.92 or higher. This is in agreement with other works ($R^2 > 0.91$ in all the references mentioned above, except in Schneider et al. (2010), where $R^2 = 0.85$ was reported for V2 AERONET data). Using radiosondes as reference, Campmany et al. (2010) performed a comparison between radiosonde and Cimel in Barcelona, showing R^2 of 0.947 for the two data-sets, while Fragkos et al. (2019) found a R^2 over 0.95. Schneider et al. (2010), however, found a lower correlation against GNSS, probably due to the use of level 1.5 sun photometer data, although this work found higher correlations between sun-photometers and other instruments (i.e., more than 0.95 with multi-filter rotating shadow-band radiometer). Thus, linear regressions show excellent agreements of Cimel AERONET with GNSS and similar to values reported in other works.

4.2. *IWV dependence*

Performance of sun-photometer IWV can vary as IWV changes itself. Fig. 2 shows the MBE (left panel) and SD (right panel) calculated over different IWV bins. The stations *acor*, *mall* show a rather stable MBE with IWV. However, the rest of stations show a decreasing MBE as IWV increases, reaching dry bias above 4 mm. The decreasing slopes in the MBE vs IWV lines go from 0.060.17. Regarding SD, the general behavior is to increase as IWV increases, in some cases saturating or even decreasing for high IWV, with slopes of 0.04–0.05. The overestimation at low IWV can be explained by the low sensitivity of GNSS to small amounts of water vapor, leading to systematic underestimation of this instrument at low values of IWV (Wang et al., 2007; Schneider et al., 2010). The general underestimation of Cimel sun-photometers under large IWV is reported in other works. For example, Fragkos et al. (2019) found a slope

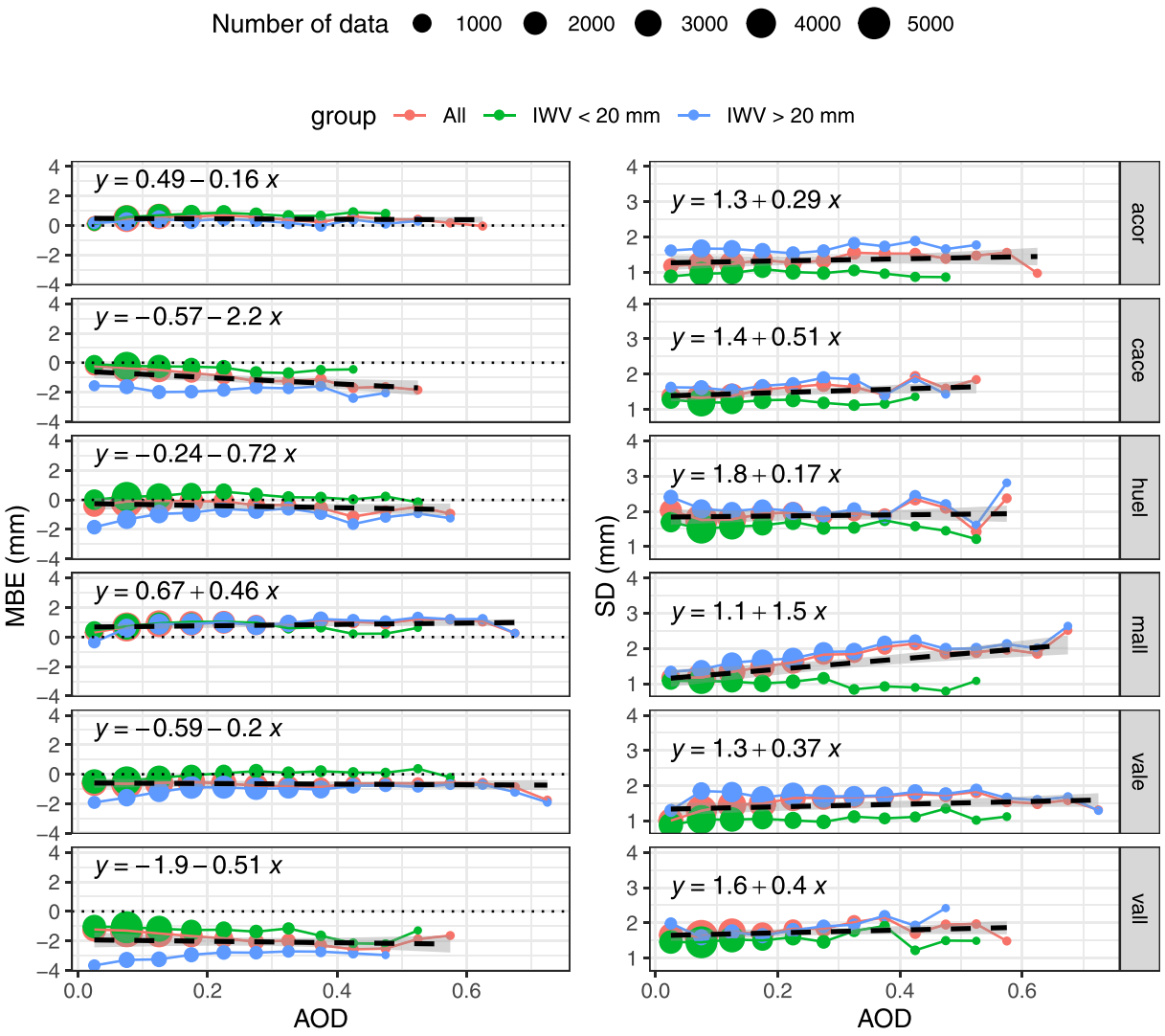

Fig. 5. MBE (left panels) and SD (right panels) along AOD 551 nm values. Dashed line represents the linear fit.

of (−0.138 ± 0.012) %mm^{-1} against microwave radiometer, which is consistent with the results found in Fig. 2.

4.3. SZA dependence

As sun-photometry deals with direct measurements of solar radiation, SZA can have an effect on its ability to retrieve IWV. On the one hand, a larger water vapor optical path can enhance its signal, but on the other hand, more noise can be induced and more sources of error when dealing with the conversion from slant to vertical water vapor column. Fig. 3 shows the MBE and SD in different SZA bins. In this case, the dataset has been divided in low IWV (IWV < 20 mm) and high IWV (IWV > 20 mm). There is not any clear pattern in the MBE, except a generalized decrease of MBE (increased dry bias) for high IWV at high SZA values. The stations *acor* and *mall* show some increase in SD with SZA for high SZA, steeper in the case of high IWV. Fragkos et al. (2019) found no clear dependence of relative differences between Cimel and radiosonde IWV data on SZA. However, that work showed an increased scatter for SZA > 70°, similarly as found in Fig. 3 of the present work. This effect might be due to the decreased amount of radiation and the increased presence of stray-light that could be affecting the direct measurements of the Cimel, resulting in an increased SD. However, it is an open issue that needs more future research.

4.4. Seasonal dependence

There can be a seasonal dependence in the performance of the IWV photometer product, as different meteorological conditions can have an effect on it. In Fig. 4 it is shown the monthly seasonal pattern of MBE and SD, divided into high and low IWV. There is not a clear pattern for MBE, although in some stations (*cace*, *vall*, and *vale*) it is observed that summer months have negative and more marked MBE than winter months. Regarding SD, summer months show an increased value of SD, while winter shows smaller values. Additionally, when comparing monthly averaged IWV with MBE and SD, a clear correlation can be observed (not shown).

Nevertheless, Prasad and Singh (2009) found an opposed seasonal pattern in India (more marked overestimation in summer than in winter) for V2 AERONET data-set. However, being India and the Iberian Peninsula two completely different climate regions, it is difficult to draw any conclusion about this disagreement. In addition, Fragkos et al. (2019) found a dependence with temperature (slope of (−0.061 ± 0.011) %°C^{-1}), which is consistent with the seasonal pattern observed in Fig. 4. It is important to note that most of these patterns seems to be related to the dependence on IWV, although the low IWV values also show the SD increase in summer, but in a weaker way.

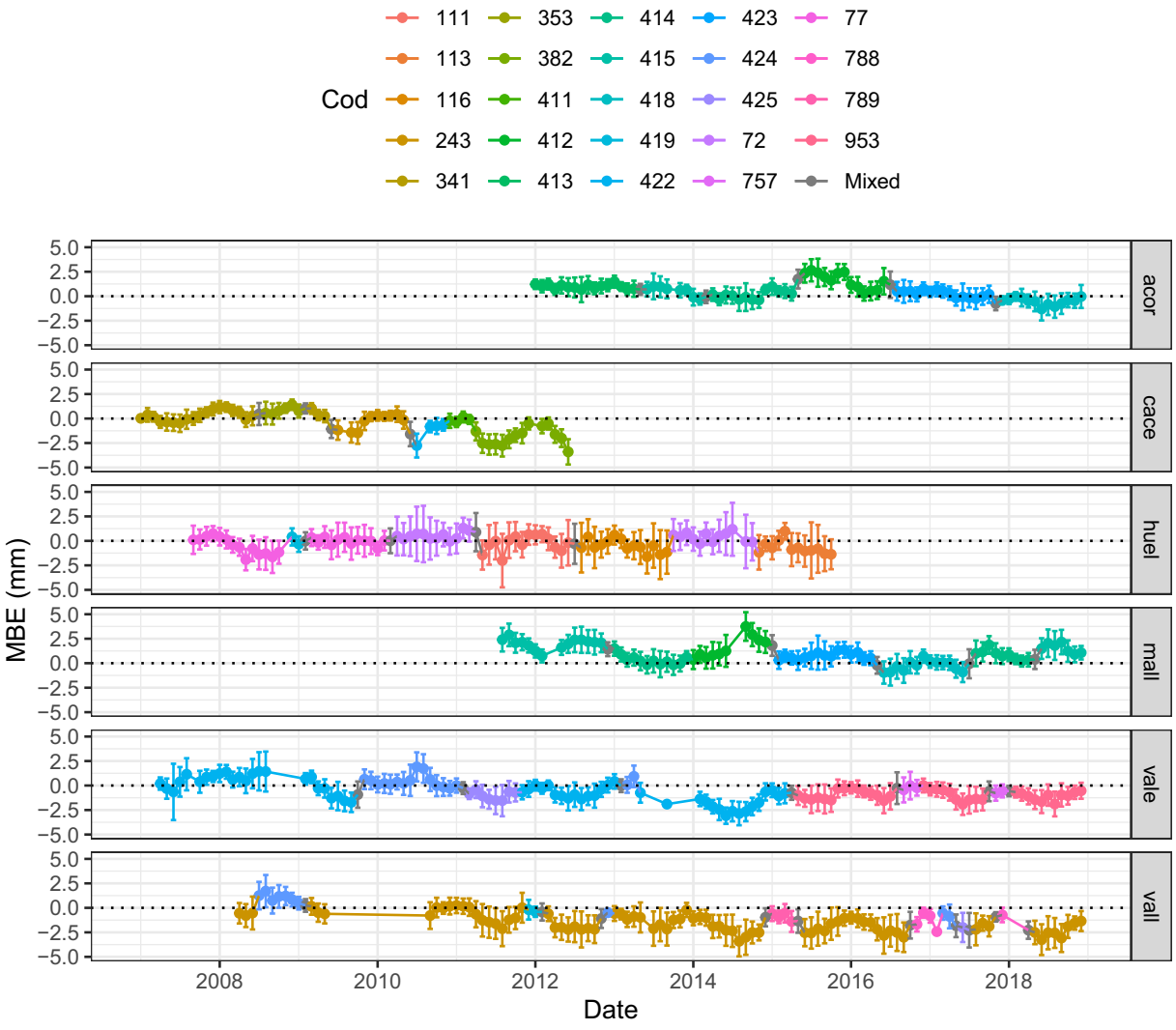

Fig. 6. MBE and monthly series. SD is marked as error bars and colors show the different devices. Cod is the device code identifier. Notice that for *huel*, the Cimel data are from El Arenosillo until March 2010, and from Huelva from March 2010.

4.5. AOD dependence

The presence of aerosols can influence the measurement of IWV with sun-photometers if aerosol transmission is not properly modeled. However, Fig. 5, which exhibits the MBE and SD in different AOD bins, shows a rather stable values of these indices along the different AOD bins. Only in *mall* station, for high IWV it is observed an increase of SD with AOD. This effect can be related to calibration issues, as the algorithm uses the AOD and IWV estimates in different bands to estimate both aerosol properties and water vapor content.

4.6. Inter-annual evolution

Different changes in instrumentation, calibration of the Cimel and trends of the aforementioned variables can induce changes in Cimel IWV performance. Therefore, Fig. 6 shows the monthly time-series of MBE and SD. The different colors mark the different Cimel devices used in each site. In some cases, the change of the device causes a change in the differences observed. For example, the use of Cimel device 412 induced wet bias in *acor* time series. This kind of problem should be taken into account when studying long time-series of Cimel and metatada must be carefully studied. It is also worth of note that some stations show a trend to underestimation as time passes (see *cace* station, for example).

5. Conclusions

This work aims to assess the quality of AERONET series of Cimel IWV in comparison with GNSS. It is observed that the correlation between the two instruments is really high ($R^2 > 0.92$). Biases are between −1.48 and 0.83 mm, and SD below 2 mm.

A clear dependence of the Cimel–GNSS differences on IWV is found. Dry bias is generally increased as IWV increases, in agreement with other works. SD of the differences also increases with IWV. The dependence on SZA is also analyzed. MBE does not show a clear pattern, but the SD increases with SZA, specially for large SZA values. These dependences (also dependence on temperature could play a role) induce a seasonal dependence on the Cimel–GNSS differences. It is observed that generally, dry bias (not in all sites) and SD are increased in summer months with respect to winter months. This may be related to the dependence on IWV mentioned above. The study of the dependence on AOD does not show a relevant influence of this variable on the Cimel–GNSS differences. Only in station *mall* and in the case of high IWV values the SD increases as AOD increases.

Finally, the inter-annual evolution of the monthly differences is analyzed in order to spot if measurements may be affected by calibration, changes of devices, or trends of the variables mentioned above. It was found that, although is not the general case, at some points the

changes of devices can induce a clear jump in the series. Also, that some stations show a slight decrease in the differences as time passes. Therefore, Cimel data should be taken with care if used for long-term changes quantification, and always making use of the available metadata to take into account possible inhomogeneity in the series.

In summary, AERONET Cimel water vapor product V3 level 2.0 shows a very good agreement with GNSS. The dependences observed must be taken into account although they are not very very important. Also, the use of metadata is highly recommended when long-term evolution is to be studied.

CRediT authorship contribution statement

Javier Vaquero-Martínez: Software, Validation, Formal analysis, Investigation, Writing – original draft, Visualization, Writing – review & editing. **André F. Bagorrilha:** Software, Formal analysis, Writing – review & editing. **Manuel Antón:** Conceptualization, Methodology, Supervision, Writing – review & editing. **Juan C. Antuña-Marrero:** Resources, Writing – review & editing. **Victoria E. Cachorro:** Resources, Supervision, Writing – review & editing.

Declaration of Competing Interest

Authors declare no conflict of insterest.

Acknowledgments

This work was supported by Junta de Extremadura (Consejería de Economía, Ciencia y Agenda Digital) and European Regional Development Fund (ERDF A Way of Making Europe), through projects GR21080 and IB18092. We thank the principal investigators and their staff for their effort in establishing and maintaining the six AERONET sites used in this investigation. We also thank EUREF for the freely available tropospheric delay data and AEMet for the temperature and pressure data needed for this work. The authors are grateful to the Spanish Ministry of Science, Innovation and Universities for the support through the ePOLAAR project (RTI2018-097864-B-I00). Thanks are due to AERONET-PHOTONS-RIMA staff for providing observations and for the maintenance of the networks.

References

Ångström, A., 1961. Techniques of Determinig the Turbidity of the Atmosphere. Tellus 13, 214–223. https://doi.org/10.1111/j.2153-3490.1961.tb00078.x.

Antuña-Marrero, J.C., Román, R., Cachorro, V.E., Mateos, D., Toledano, C., Calle, A., Antuña-Sánchez, J.C., Vaquero-Martínez, J., Antón, M., de Frutos Baraja, Á.M., 2022. Integrated water vapor over the Arctic: Comparison between radiosondes and sun photometer observations. Atmos. Res. 270, 106059 https://doi.org/10.1016/j.atmosres.2022.106059.

Bennouna, Y.S., Torres, B., Cachorro, V.E., de Galisteo, J.P.O., Toledano, C., 2013. The evaluation of the integrated water vapour annual cycle over the Iberian Peninsula from EOS-MODIS against different ground-based techniques. Q. J. R. Meteorol. Soc. 139, 1935–1956. https://doi.org/10.1002/qj.2080.

Bevis, M., Businger, S., Herring, T.A., Rocken, C., Anthes, R.A., Ware, R.H., 1992. GPS meteorology: Remote sensing of atmospheric water vapor using the global positioning system. J. Geophys. Res. 97, 15787. https://doi.org/10.1029/92JD01517.

Bevis, M., Businger, S., Chiswell, S., Herring, T.A., Anthes, R.A., Rocken, C., Ware, R.H., 1994. GPS Meteorology: Mapping Zenith Wet Delays onto Precipitable Water. J. Appl. Meteorol. 33, 379–386. https://doi.org/10.1175/1520-0450(1994)033<0379:GMMZWD>2.0.CO;2.

Bock, O., Nuret, M., 2009. Verification of NWP model analyses and radiosonde humidity data with GPS precipitable water vapor estimates during AMMA. Weather Forecast. 24, 1085–1101. https://doi.org/10.1175/2009WAF2222239.1.

Bock, O., Bosser, P., Flamant, C., Doerflinger, E., Jansen, F., Fages, R., Bony, S., Schnitt, S., 2021. Integrated water vapour observations in the Caribbean arc from a network of ground-based GNSS receivers during EUREC4A. Earth System Science Data 13, 2407–2436. https://doi.org/10.5194/essd-13-2407-2021.

Bruegge, C.J., Conel, J.E., Green, R.O., Margolis, J.S., Holm, R.G., Toon, G., 1992. Water vapor column abundance retrievals during FIFE. J. Geophys. Res. 97, 18759. https://doi.org/10.1029/92JD01050.

Buehler, S.A., Östman, S., Melsheimer, C., Holl, G., Eliasson, S., John, V.O., Blumenstock, T., Hase, F., Elgered, G., Raffalski, U., Nasuno, T., Satoh, M., Milz, M., Mendrok, J., 2012. A multi-instrument comparison of integrated water vapour measurements at a high latitude site. Atmos. Chem. Phys. 12, 10925–10943. https://doi.org/10.5194/acp-12-10925-2012.

Campmany, E., Bech, J., Rodríguez-Marcos, J., Sola, Y., Lorente, J., 2010. A comparison of total precipitable water measurements from radiosonde and sunphotometers. Atmos. Res. 97, 385–392. https://doi.org/10.1016/j.atmosres.2010.04.016.

Carbajal Henken, C., Dirks, L., Steinke, S., Diedrich, H., August, T., Crewell, S., 2020. Assessment of sampling effects on various satellite-derived integrated water vapor datasets using GPS measurements in germany as reference. Remote Sens. 12, 1170. https://doi.org/10.3390/rs12071170.

Colman, R., 2003. A comparison of climate feedbacks in general circulation models. Clim. Dyn. 20, 865–873. https://doi.org/10.1007/s00382-003-0310-z.

Colman, R.A., 2015. Climate radiative feedbacks and adjustments at the Earth's surface. Journal of Geophysical Research: Atmospheres 120, 3173–3182. https://doi.org/10.1002/2014JD022896.

Cucurull, L., Navascues, B., Ruffini, G., Elósegui, P., Rius, A., Vilà, J., 2000. The use of GPS to validate NWP Systems: the HIRLAM model. J. Atmos. Ocean. Technol. 17, 773–787. https://doi.org/10.1175/1520-0426(2000)017<0773:TUOGTV>2.0.CO;2.

Davis, J.L., Herring, T.A., Shapiro, I.I., Rogers, A.E.E., Elgered, G., 1985. Geodesy by radio interferometry: Effects of atmospheric modeling errors on estimates of baseline length. Radio Sci. 20, 1593–1607. https://doi.org/10.1029/RS020i006p01593.

Elgered, G., Davis, J.L., Herring, T.A., Shapiro, I.I., 1991. Geodesy by radio interferometry: Water vapor radiometry for estimation of the wet delay. Journal of Geophysical Research: Solid Earth 96, 6541–6555. https://doi.org/10.1029/90JB00834.

Fragkos, K., Antonescu, B., Giles, D.M., Ene, D., Boldeanu, M., Efstathiou, G.A., Belegante, L., Nicolae, D., 2019. Assessment of the total precipitable water from a sun photometer, microwave radiometer and radiosondes at a continental site in southeastern Europe. Atmospheric Measurement Techniques 12, 1979–1997. https://doi.org/10.5194/amt-12-1979-2019.

García, R.D., Cuevas, E., Cachorro, V.E., García, O.E., Barreto, Á., Almansa, A.F., Romero-Campos, P.M., Ramos, R., Pó, M., Hoogendijk, K., Gross, J., 2021. Water Vapor Retrievals from Spectral Direct Irradiance measured with an EKO MS-711 Spectroradiometer—Intercomparison with Other Techniques. Remote Sens. 13, 350. https://doi.org/10.3390/rs13030350.

Giles, D.M., Sinyuk, A., Sorokin, M.G., Schafer, J.S., Smirnov, A., Slutsker, I., Eck, T.F., Holben, B.N., Lewis, J.R., Campbell, J.R., Welton, E.J., Korkin, S.V., Lyapustin, A.I., 2019. Advancements in the Aerosol Robotic Network (AERONET) Version 3 database – automated near-real-time quality control algorithm with improved cloud screening for Sun photometer aerosol optical depth (AOD) measurements. Atmospheric Measurement Techniques 12, 169–209. https://doi.org/10.5194/amt-12-169-2019.

Gong, S., Hagan, D.F.T., Zhang, C., 2019. Analysis on Precipitable Water Vapor over the Tibetan Plateau using FengYun-3A Medium Resolution Spectral Imager Products. Journal of Sensors 2019, 1–12. https://doi.org/10.1155/2019/6078591.

Halthore, R., Markham, B., Deering, D., 1992. Atmospheric correction and calibration during Kurex-91. In: [Proceedings] IGARSS '92 International Geoscience and Remote Sensing Symposium, vol. 2. IEEE, Houston, TX, pp. 1278–1280. https://doi.org/10.1109/IGARSS.1992.578413.

Hansen, J.E., Travis, L.D., 1974. Light scattering in planetary atmospheres. Space Sci. Rev. 16, 527–610. https://doi.org/10.1007/BF00168069.

Holben, B., Eck, T., Slutsker, I., Tanré, D., Buis, J., Setzer, A., Vermote, E., Reagan, J., Kaufman, Y., Nakajima, T., Lavenu, F., Jankowiak, I., Smirnov, A., 1998. AERONET—A Federated Instrument Network and Data Archive for Aerosol Characterization. Remote Sens. Environ. 66, 1–16. https://doi.org/10.1016/S0034-4257(98)00031-5.

Kasten, F., 1965. A new table and approximation formula for the relative optial air mass. Archiv für Meteorologie, Geophysik und Bioklimatologie Serie B 14, 206–223. https://doi.org/10.1007/BF02248840.

Kasten, F., Young, A.T., 1989. Revised optical air mass tables and approximation formula. Appl. Opt. 28, 4735. https://doi.org/10.1364/AO.28.004735.

Köpken, C., 2001. Validation of integrated water vapor from numerical models using ground-based GPS, SSM/I, and water vapor radiometer measurements. J. Appl. Meteorol. 40, 1105–1117. https://doi.org/10.1175/1520-0450(2001)040<1105:VOIWVF>2.0.CO;2.

Matsuyama, H., Flores, J., Oikawa, K., Miyaoka, K., 2020. Comparison of precipitable water via JRA-55 and GPS in Japan considering different elevations. Hydrological Research Letters 14, 9–16. https://doi.org/10.3178/hrl.14.9.

Morland, J., Collaud Coen, M., Hocke, K., Jeannet, P., Mätzler, C., 2009. Tropospheric water vapour above Switzerland over the last 12 years. Atmos. Chem. Phys. https://doi.org/10.7892/BORIS.37604.

Myhre, G., Shindell, D., Bréon, F.-M., Collins, W., Fuglestvedt, J., Huang, J., Koch, D., Lamarque, J.-F., Lee, D., Mendoza, B., Nakajima, T., Robock, A., Stephens, G., Takemura, T., Zhang, H., 2013. Anthropogenic and Natural Radiative Forcing. In: Climate Change 2013: The Physical Science Basis. Contribution of Working Group I to the Fifth Assessment Report of the Intergovernmental Panel on Climate Change. IPCC, pp. 659–740 (Ipcc ed.).

Ningombam, S.S., Jade, S., Shrungeshwara, T., Song, H.-J., 2016. Validation of water vapor retrieval from Moderate Resolution Imaging Spectro-radiometer (MODIS) in near infrared channels using GPS data over IAO-Hanle, in the trans-Himalayan region. J. Atmos. Sol. Terr. Phys. 137, 76–85. https://doi.org/10.1016/j.jastp.2015.11.019.

Ortiz de Galisteo, J.P., Toledano, C., Cachorro, V., Torres, B., 2010. Improvement in PWV estimation from GPS due to the absolute calibration of antenna phase center

variations. GPS Solutions 14, 389–395. https://doi.org/10.1007/s10291-010-0163-y.
Ortiz de Galisteo, J.P., Cachorro, V., Toledano, C., Torres, B., Laulainen, N., Bennouna, Y., de Frutos, A., 2011. Diurnal cycle of precipitable water vapor over Spain. Q. J. R. Meteorol. Soc. 137, 948–958. https://doi.org/10.1002/qj.811.
Pérez-Ramírez, D., Whiteman, D.N., Smirnov, A., Lyamani, H., Holben, B.N., Pinker, R., Andrade, M., Alados-Arboledas, L., 2014. Evaluation of AERONET precipitable water vapor versus microwave radiometry, GPS, and radiosondes at ARM sites. Journal of Geophysical Research: Atmospheres 119, 9596–9613. https://doi.org/10.1002/2014JD021730.
Prasad, A.K., Singh, R.P., 2009. Validation of MODIS Terra, AIRS, NCEP/DOE AMIP-II Reanalysis-2, and AERONET Sun photometer derived integrated precipitable water vapor using ground-based GPS receivers over India. J. Geophys. Res. 114, D05107. https://doi.org/10.1029/2008JD011230.
Raja, M.K.R.V., Gutman, S.I., Yoe, J.G., McMillin, L.M., Zhao, J., 2008. The Validation of AIRS Retrievals of Integrated Precipitable Water Vapor using Measurements from a Network of Ground-Based GPS Receivers over the Contiguous United States. J. Atmos. Ocean. Technol. 25, 416–428. https://doi.org/10.1175/2007JTECHA889.1.
Román, R., Antón, M., Cachorro, V., Loyola, D., Ortiz de Galisteo, J., de Frutos, A., Romero-Campos, P., 2015. Comparison of total water vapor column from GOME-2 on MetOp-A against ground-based GPS measurements at the Iberian Peninsula. Sci. Total Environ. 533, 317–328. https://doi.org/10.1016/j.scitotenv.2015.06.124.
Saastamoinen, J., 1972. Atmospheric Correction for the Troposphere and Stratosphere in Radio Ranging Satellites. In: Henriksen, S.W., Mancini, A., Chovitz, B.H. (Eds.), Geophysical Monograph Series. American Geophysical Union, Washington, D. C, pp. 247–251. https://doi.org/10.1029/GM015p0247.
Schneider, M., Romero, P.M., Hase, F., Blumenstock, T., Cuevas, E., Ramos, R., 2010. Continuous quality assessment of atmospheric water vapour measurement techniques: FTIR, Cimel, MFRSR, GPS, and Vaisala RS92. Atmospheric Measurement Techniques 3, 323–338. https://doi.org/10.5194/amt-3-323-2010.
Vaquero-Martínez, J., Antón, M., 2021. Review on the Role of GNSS Meteorology in monitoring Water Vapor for Atmospheric Physics. Remote Sens. 13, 2287. https://doi.org/10.3390/rs13122287.
Vaquero-Martínez, J., Antón, M., Ortiz de Galisteo, J.P., Cachorro, V.E., Costa, M.J., Román, R., Bennouna, Y.S., 2017a. Validation of MODIS integrated water vapor product against reference GPS data at the Iberian Peninsula. Int. J. Appl. Earth Obs. Geoinf. 63, 214–221. https://doi.org/10.1016/j.jag.2017.07.008.
Vaquero-Martínez, J., Antón, M., Ortiz de Galisteo, J.P., Cachorro, V.E., Wang, H., González Abad, G., Román, R., Costa, M.J., 2017b. Validation of integrated water vapor from OMI satellite instrument against reference GPS data at the Iberian Peninsula. Sci. Total Environ. 580, 857–864. https://doi.org/10.1016/j.scitotenv.2016.12.032.
Vaquero-Martínez, J., Antón, M., Ortiz de Galisteo, J.P., Cachorro, V.E., Álvarez-Zapatero, P., Román, R., Loyola, D., Costa, M.J., Wang, H., Abad, G.G., Noël, S., 2018. Inter-comparison of integrated water vapor from satellite instruments using reference GPS data at the Iberian Peninsula. Remote Sens. Environ. 204, 729–740. https://doi.org/10.1016/j.rse.2017.09.028.
Vaquero-Martínez, J., Antón, M., Román, R., Cachorro, V.E., Wang, H., González Abad, G., Ritter, C., 2020. Water vapor satellite products in the European Arctic: an inter-comparison against GNSS data. Sci. Total Environ. 741, 140335 https://doi.org/10.1016/j.scitotenv.2020.140335.
Wang, J., Zhang, L., Dai, A., Van Hove, T., Van Baelen, J., 2007. A near-global, 2-hourly data set of atmospheric precipitable water from ground-based GPS measurements. J. Geophys. Res. 112, D11107. https://doi.org/10.1029/2006JD007529.
Wang, H., Gonzalez Abad, G., Liu, X., Chance, K., 2016. Validation and update of OMI Total Column Water Vapor product. Atmos. Chem. Phys. 16, 11379–11393. https://doi.org/10.5194/acp-16-11379-2016.
Wang, H., Souri, A.H., González Abad, G., Liu, X., Chance, K., 2019. Ozone monitoring Instrument (OMI) Total Column Water Vapor version 4 validation and applications. Atmospheric Measurement Techniques 12, 5183–5199. https://doi.org/10.5194/amt-12-5183-2019.
Yang, X., Sass, B.H., Elgered, G., Johansson, J.M., Emardson, T.R., 1999. A comparison of precipitable water vapor estimates by an NWP simulation and GPS observations. J. Appl. Meteorol. Climatol. 38, 941–956. https://doi.org/10.1175/1520-0450(1999)038<0941:ACOPWV>2.0.CO;2.